

# Large-scale aircraft design using SU2

Francisco Palacios\*, Thomas D. Economon†, Andrew D. Wendorff‡, and Juan J. Alonso§  
*Stanford University, Stanford, CA, 94305, U.S.A.*

This paper discusses the use of the continuous adjoint methodology for the design of transonic aircraft configurations. The objective of the present study is to illustrate that, despite the fact that continuous adjoint does not provide the numerically exact gradient of a discrete objective function, it is an excellent choice for large-scale optimization with complex geometries due to the accuracy of the computed gradients, the robustness of the method, and its efficiency in terms of memory and compute time. This is demonstrated through a series of detailed design studies on the NASA Common Research Model, which provides a challenging problem due to its geometric complexity and the large, unstructured meshes employed. All design work is completed with the SU2 software suite: an open-source, integrated analysis and design tool for solving complex, multi-disciplinary problems on unstructured computational grids.

## I. Introduction

The solution of the Reynolds-averaged Navier-Stokes (RANS) equations around complete aircraft configurations on computational meshes containing millions of elements is now an everyday occurrence in the aerospace industry.<sup>1</sup> Efficient algorithms for Computational Fluid Dynamics (CFD) have allowed the aerospace industry to perform large numbers of simulations for rapidly evaluating candidate designs. Other developments, such as unstructured mesh technology, have enabled the analysis of increasingly complex geometries. Given the shorter turnaround times afforded by advances in CFD, applying optimal shape design techniques to large-scale problems of industrial interest with complex geometry is increasingly tractable.

It is now well established that, due to the high cost of solving the nonlinear flow equations and the large design spaces that typically accompany aerodynamic shape design problems, gradient-based optimization methods coupled with adjoint techniques for sensitivity analysis offer the most efficient process for shape design. In the academic sense, these tools, and adjoint methods in particular, have become relatively mature over the last quarter-century for problems in aeronautics. However, their adoption for realistic problems in industrial settings has lagged due to difficulties related to robustness, accuracy, or an inability to handle the large, complex meshes required for representing detailed aircraft configurations due to memory or compute overheads.

In our opinion, this situation merits a renewed focus on techniques that offer the additional flexibility to overcome these roadblocks, while also providing sufficient accuracy and computational performance. In particular, the methods should contain customizable numerical methods in order to alleviate convergence issues and must be able to leverage modern high-performance computing resources to maintain turnaround times that fit well within the industrial design cycle.

For problems in aeronautics, Jameson first introduced the adjoint approach for shape design in transonic flows to reduce shock-induced drag.<sup>2,3</sup> Further pioneering work by Jameson et al.<sup>4,5</sup> treated the Euler and Navier-Stokes equations in three dimensions, thus enabling the design of complete aircraft configurations.<sup>6</sup> Adjoint formulations as a means of sensitivity analysis have since become the subject of a rich volume of research literature, but again, their practical application to large-scale problems with complex geometries appears to have stalled.<sup>7</sup>

\*Engineering Research Associate, Department of Aeronautics & Astronautics, AIAA Senior Member.

†Postdoctoral Scholar, Department of Aeronautics & Astronautics, AIAA Senior Member.

‡Ph.D. Candidate, Department of Aeronautics & Astronautics, AIAA Student Member.

§Associate Professor, Department of Aeronautics & Astronautics, AIAA Associate Fellow.

Fortunately, a number of recent advances are ushering in a new era for the continuous adjoint methodology and broadening its range of applicability. While initial results for the continuous adjoint were calculated on structured meshes, numerical methods for the continuous adjoint equations were extended to unstructured meshes for complex geometries. Anderson and Venkatakrishnan<sup>8</sup> demonstrated one of the first surface formulations (i.e., an analytic expression for the variation of the cost function as a surface integral) for the Navier-Stokes equations on unstructured meshes, but they noted that higher-order derivative terms appearing in the adjoint equations caused issues related to implementation and accuracy. Jameson and Kim<sup>9</sup> arrived at a similar surface formulation for the Euler equations by eliminating volume integral terms from the gradient formula in the continuous limit.

Castro et al.<sup>10</sup> derived continuous adjoints for inviscid and laminar flows on unstructured grids with a special emphasis on simplifications and the reduction of higher-order derivative terms with the aid of differential geometry formulas (shape calculus).<sup>11,12</sup> The resulting surface formulation alleviated many of the issues related to implementation and accuracy for unstructured meshes, and it has been successfully applied on three-dimensional meshes for a range of applications.<sup>13,14</sup> Bueno-Orovio et al.<sup>15</sup> later extended the formulation to turbulent flows by including the Spalart-Allmaras (S-A) turbulence model, which represented the first such formulation for compressible flows.

This type of continuous adjoint methodology embodies a number of the qualities that we desire when attempting large-scale shape design. In particular, obtaining a surface formulation for shape design gradients, the ability to tailor numerical solution methods for the adjoint equations (to help mitigate numerical stiffness), and low overhead in terms of compute and memory (since much of the same code infrastructure and numerical methods can be reused from the primal problem) make the continuous adjoint approach particularly attractive. To summarize, the main contributions of this article are the demonstration of the continuous adjoint and the discussion of the procedure when redesigning the NASA CRM for improved aerodynamic performance (drag reduction) in a number of scenarios that include realistic constraints on the geometry, lift, and moments.

The paper is organized as follows. Section II contains an overview of the theory behind each major component of the shape design framework: the governing flow equations, the continuous adjoint methodology, the optimization framework, and the design variable definition. Section III contains a description of the NASA CRM along with a brief verification and validation study before detailing a series of redesign studies for the CRM that illustrate the effectiveness of the continuous adjoint methodology in this setting. Lastly, Section IV summarizes the main conclusions of the article.

## II. Description of the shape optimization technique

### A. Governing system of equations

The Navier-Stokes equations<sup>16,17</sup> describe the conservation of mass, momentum and energy in a viscous fluid. Aeronautical applications assume that the air is governed by these equations on a domain  $\Omega \subset \mathbb{R}^3$ , delimited by disconnected boundaries divided into a “far field”,  $\Gamma_\infty$ , and solid (adiabatic in this paper) walls that we denote by  $S$ . Their steady-state formulation can be written in the following form<sup>15</sup>

$$\begin{cases} R_U(U) = \nabla \cdot \vec{F}^c - \nabla \cdot (\mu_{tot}^1 \vec{F}^{v1} + \mu_{tot}^2 \vec{F}^{v2}) = 0 & \text{in } \Omega, \\ \vec{v} = 0 & \text{on } S, \\ \partial_n T = 0 & \text{on } S, \\ (W)_+ = W_\infty & \text{on } \Gamma_\infty, \end{cases} \quad (1)$$

where  $U = (\rho, \rho v_1, \rho v_2, \rho v_3, \rho E)^\top$  stands for the vector of conservative variables,  $\rho$  is the density,  $E$  is the energy,  $\vec{v} = (v_1, v_2, v_3) \in \mathbb{R}^3$  is the flow speed in a Cartesian system of reference, and  $T$  is the temperature. The last equation in (1) represents classical “far field” boundary conditions simulating the fluid behavior at infinity. The vectors  $\vec{F}^c(U) = (\vec{F}_1^c, \vec{F}_2^c, \dots, \vec{F}_5^c)^\top$  are the convective fluxes and  $\vec{F}^{vk}(U) = (\vec{F}_1^{vk}, \vec{F}_2^{vk}, \dots, \vec{F}_5^{vk})^\top$ ,  $k = 1, 2$ , are the viscous fluxes, in where we have considered separately the contribution of the viscous forces and the heat flux transfer. Here,  $(\cdot)^\top$  denotes transposition.

As usual in turbulence modeling based upon the Boussinesq hypothesis,<sup>18</sup> which states that the effect of turbulence can be represented as an increased viscosity, the viscosity is divided into a laminar  $\mu_{dyn}$  and a turbulent  $\mu_{tur}$  component. The laminar or dynamic viscosity is usually taken to be only dependent on the

temperature,  $\mu_{dyn} = \mu_{dyn}(T)$ , whereas  $\mu_{tur}$  is obtained from a suitable turbulence model involving the flow and a set of new variables. Turbulence and main stream flow become then coupled by replacing the dynamic viscosity in the momentum and energy equations in the Navier-Stokes equations with

$$\mu_{tot}^1 = \mu_{dyn} + \mu_{tur}, \quad \mu_{tot}^2 = \frac{\mu_{dyn}}{Pr_d} + \frac{\mu_{tur}}{Pr_t} \quad (2)$$

where  $Pr_d$  and  $Pr_t$  are respectively the dynamic and turbulent Prandtl numbers. Here  $\mu_{tot}^2$  represents the effective thermal conductivity that we write in this nonstandard notation to obtain reduced expressions in the calculus below.

The systems (1) with a suitable equation of state to describe the fluid thermodynamics, constitute a complete system of equations and boundary conditions for the flow variables.<sup>18,19</sup>

## B. Definition of the objective function

A key element for the definition of an optimal shape design problem is the objective function. In this case, we introduce an objective function which is assumed to be only dependent on the values of the flow variables at the boundary  $S$ . As it was shown in,<sup>20</sup> for the Navier-Stokes system only objective functions depending on  $\vec{f}$  and the temperature  $T$  are allowed for continuous adjoint optimization, with  $\vec{f}$  given by

$$\vec{f} = (f_1, f_2, f_3) = P\vec{n} - \bar{\sigma} \cdot \vec{n}, \quad \bar{\sigma} = \mu_{tot}^1 \bar{\tau} \quad (3)$$

where  $\vec{n}$  denotes the exterior normal to the surface  $S$ ,  $P$  is the pressure of the fluid, and  $\bar{\sigma}$  the second order tensor of viscous stresses,  $\bar{\tau}$  given in Appendix A. Note that this includes, in particular, functionals depending only on the pressure  $P$  since it can be written as a function of  $\vec{f}$ , using the fact that  $\vec{n} \cdot \bar{\sigma} \cdot \vec{n} = 0$  on the boundary.<sup>20</sup> More precisely,

$$P = \vec{n} \cdot (P\vec{n} - \bar{\sigma} \cdot \vec{n}) = \vec{f} \cdot \vec{n} \quad \text{on } S. \quad (4)$$

For the purposes of the present study, we will consider the following general choice of force based objective function

$$J(S) = \int_S j(\vec{f}, T, \vec{n}) ds. \quad (5)$$

## C. Variation of the objective function: the adjoint approach

As usual in the adjoint approach,<sup>4,8,15,20,21</sup> flow equations are incorporated to the cost functional as constraints by means of a Lagrange multiplier for each equation,  $\Psi_U^\top = (\psi_1, \psi_2, \psi_3, \psi_4, \psi_5)$ . In this way, the Lagrangian reads

$$\mathcal{J}(S) = \int_S j(\vec{f}, T, \vec{n}) ds + \int_\Omega \Psi_U^\top R_U(U) d\Omega. \quad (6)$$

Let us consider an arbitrary (but small) perturbation of the boundary  $S$  which, without loss of generality, can be parameterized by an infinitesimal deformation of size  $\delta S$  along the normal direction to the surface  $S$ . The new surface obtained after the deformation is then given by

$$S' = \{\vec{x} + \delta S \vec{n}, \vec{x} \in S\} \quad (7)$$

where, for small deformations, the following holds<sup>22</sup>

$$\begin{cases} \delta \vec{n} = -\nabla_S(\delta S) \\ \delta(ds) = -2H_m \delta S ds \end{cases} \quad (8)$$

where  $H_m$  is the mean curvature of  $S$  computed as  $(\kappa_1 + \kappa_2)/2$ , and  $(\kappa_1, \kappa_2)$  are curvatures in two orthogonal directions on the surface. Here  $\nabla_S$  represents the tangential gradient operator on  $S$ . Note that  $\nabla_S(\delta S)$  is a tangent vector to  $S$  that we write as a vector in  $\mathbb{R}^3$  with null component normal to  $S$ .

Assuming a regular flow solution  $U$  and a smooth boundary  $S$ , the variation of the functional  $J$  due to the deformation can be evaluated as

$$\delta \mathcal{J} = \int_S \delta j(\vec{f}, T, \vec{n}) ds + \int_{\delta S} j(\vec{f}, T, \vec{n}) ds + \int_\Omega \Psi_U^\top \delta R_U(U) d\Omega \quad (9)$$

where  $\delta R_U$  represents the variations of  $R_U$ , respectively. Using the convention of summation of repeated indexes,  $i = 1, 2, 3$ , the two first terms in the previous equation read

$$\int_S \delta j(\vec{f}, T, \vec{n}) ds = \int_S \frac{\partial j}{\partial \vec{f}} \cdot (\delta P \vec{n} - \delta \bar{\sigma} \cdot \vec{n}) + \frac{\partial j}{\partial T} \delta T - \left( \frac{\partial j}{\partial \vec{n}} + \frac{\partial j}{\partial \vec{f}} P - \frac{\partial j}{\partial \vec{f}} \cdot \bar{\sigma} \right) \cdot \nabla_S(\delta S) ds \quad (10)$$

$$\int_{\delta S} j(\vec{f}, T, \vec{n}) ds = \int_S \left( \frac{\partial j}{\partial f_i} \partial_n f_i + \frac{\partial j}{\partial T} \partial_n T - 2H_m j \right) \delta S ds. \quad (11)$$

Note that in (10) we have written the variation  $\delta \vec{f}$  in terms of  $\delta P$  and  $\delta \bar{\sigma}$ , and we have used formula (8) for  $\delta \vec{n}$ . The variations  $\delta P \vec{n} - \delta \bar{\sigma} \cdot \vec{n}$  and  $\delta T$  appearing in (10) can be computed from the following linearized system

$$\begin{cases} \delta R_U(U) = \frac{\partial R_U}{\partial U} \delta U = 0 & \text{in } \Omega, \\ \delta \vec{v} = -\partial_n \vec{v} \delta S & \text{on } S, \\ \partial_n(\delta T) = (\nabla T) \cdot \nabla_S(\delta S) - \partial_n^2 T \delta S & \text{on } S, \\ (\delta W)_+ = 0 & \text{on } \Gamma_\infty, \end{cases} \quad (12)$$

where  $(\delta W)_+$  represents the incoming characteristics on the “far field” boundary. Linearization of the Navier-Stokes is respectively given in Appendix B.

Domain integrals in (9) are eliminated using integration by parts and introducing the associated adjoint operators. This integration by parts also provides some boundary terms, which are combined with the boundary terms in (9) depending on  $\delta P \vec{n} - \delta \bar{\sigma} \cdot \vec{n}$  and  $\delta T$ , yielding the boundary conditions for the adjoint operators. We describe this process below.

From (12), the last term in (9) reads

$$\int_\Omega \Psi_U^\top \left( \frac{\partial R_U}{\partial U} \delta U \right) = \int_\Omega (A_U \Psi_U)^\top \delta U + \int_S B_S ds \quad (13)$$

where  $A_U = \left( \frac{\partial R_U}{\partial U} \right)^\top$  is the adjoint operators and  $B_S$  stands for the boundary terms coming from the integration by parts

$$\int_S B_S ds = - \int_S \vec{\varphi} \cdot (\delta P \vec{n} - \delta \bar{\sigma} \cdot \vec{n}) ds - \int_S (\vec{g}_1 \cdot \vec{\varphi} + g_2 \partial_n \psi_5) \delta T ds - \int_S \hat{g} \delta S ds \quad (14)$$

where  $\vec{\varphi} = (\psi_2, \psi_3, \psi_4)$  and  $\vec{g}_1$ ,  $g_2$  and  $\hat{g}$  are some functions that do not depend on the adjoint variables  $\Psi_U$ . The analytical expression of these terms and the adjoint operators above are given in in Appendix C.

In order to eliminate domain integrals in (9) when replacing the last three terms by using (13), we assume that the adjoint variables satisfy

$$A_U \Psi_U = 0 \quad (15)$$

Analogously, all boundary terms in (13) without explicit dependence on  $\delta S$  can be eliminated by considering the following choice of boundary conditions for the adjoint variables

$$\begin{cases} \varphi_i = \frac{\partial j}{\partial f_i} & \text{on } S, \\ \partial_n \psi_5 = \frac{1}{g_2} \left( \frac{\partial j}{\partial T} + \vec{g}_1 \cdot \vec{\varphi} \right) & \text{on } S, \end{cases} \quad (16)$$

Combining (9)-(11), (13)-(14), the adjoint equation (15) and the boundary conditions in (16), we finally obtain

$$\begin{aligned} \delta \mathcal{J} &= \int_S \left( \frac{\partial j}{\partial f_i} \partial_n f_i + \frac{\partial j}{\partial T} \partial_n T \right) \delta S ds \\ &\quad - \int_S \left( \frac{\partial j}{\partial \vec{n}} + \frac{\partial j}{\partial \vec{f}} P - \frac{\partial j}{\partial \vec{f}} \cdot \bar{\sigma} \right) \cdot \nabla_S(\delta S) ds - \int_S (\hat{g} + 2H_m j) \delta S ds. \end{aligned} \quad (17)$$

In this expression, the adjoint variables are obtained by solving the closed system of PDEs and boundary conditions given by (15). Some particular but still interesting situations provide a more simplified formula

for the variation of  $J$ , as described in<sup>20</sup> for the Navier-Stokes equations. Assume that the objective function depends only on  $\vec{f}$  in the following way

$$j(\vec{f}) = \vec{f} \cdot \vec{d} \quad (18)$$

where  $\vec{d}$  is a constant vector (the choice  $\vec{d} = \vec{n}$  is also possible with some modifications, but for simplicity we focus on constant  $\vec{d}$ ). Note that this is the case in drag or lift optimization problems. The adjoint boundary conditions in this situation simply become

$$\begin{cases} \vec{\varphi} = \vec{d} & \text{on } S, \\ \partial_n \psi_5 = \vec{g}_1 \cdot \vec{d}/g_2 & \text{on } S, \end{cases} \quad (19)$$

and the variation of  $J$  is given by

$$\delta J = \int_S \vec{d} \cdot \partial_n f_i \delta S \, ds - \int_S (P\vec{d} - \vec{d} \cdot \vec{\sigma}) \cdot \nabla_S (\delta S) \, ds - \int_S (\hat{g} + 2H_m j) \delta S \, ds. \quad (20)$$

Integrating now by parts, and assuming that either  $S$  is smooth or  $\delta S = 0$  at its singular points, yields

$$\begin{aligned} \delta J &= \int_S \partial_n (P\vec{d} \cdot \vec{n} - \vec{d} \cdot \vec{\sigma} \cdot \vec{n}) \delta S \, ds + \int_S \nabla_S \cdot (P\vec{d} - \vec{d} \cdot \vec{\sigma}) \delta S \, ds - \int_S (\hat{g} + 2H_m j) \delta S \, ds \\ &= \int_S \nabla \cdot (P\vec{d} - \vec{d} \cdot \vec{\sigma}) \delta S \, ds - \int_S \hat{g} \delta S \, ds = - \int_S \hat{g} \delta S \, ds. \end{aligned} \quad (21)$$

Here we have used the fact that the divergence operator, on local coordinates of  $S$ , is given by

$$\nabla \cdot \vec{q} = \partial_n (\vec{q} \cdot \vec{n}) + \nabla_S \cdot \vec{q} - 2H_m \vec{q} \cdot \vec{n} \quad (22)$$

for a general vector field  $\vec{q}$ , and the identity

$$\nabla \cdot (P\vec{d} - \vec{d} \cdot \vec{\sigma}) = (\nabla P - \nabla \cdot \vec{\sigma}) \cdot \vec{d} = 0 \quad \text{on } S, \quad (23)$$

which is obtained assuming that the momentum equations in the Navier-Stokes system are satisfied on the boundary, i.e.  $\nabla P = \nabla \cdot \vec{\sigma}$  on  $S$ .

The final expression for the total variation of the functional can be simplified as follows

$$\delta J = \int_S (\vec{n} \cdot \bar{\Sigma}^\varphi \cdot \partial_n \vec{v} - \mu_{tot}^2 C_p \nabla_S \psi_5 \cdot \nabla_S T) \delta S \, ds \quad (24)$$

with  $\bar{\Sigma}^\varphi$  depending on the gradient of the adjoint variables  $\vec{\varphi}$ . Note that we are supposing a smooth flow solution; a complete Euler adjoint formulation with shock waves can be found in Ref.<sup>23</sup>

## D. Optimization Framework

The iterative Modification methods are based in a powerful idea: modify the shape of the body during the optimization process until it is not possible to improve the value of an objective function satisfying some constraints. In other words, these methods are based on an iterative modification of the shape of the body until the convergence of a particular figure of merit is observed. Depending of the method itself the designer should provide value of the objective function and/or gradients and Hessians. Iterative Modification Methods require the detailed definition of the design variables, the objective function and a set of constraints functions:

- The vector of design variables  $\bar{x} \in \mathbb{R}^n$  with  $n > 0$  represents the geometrical changes in the surface.  $\bar{x}$  is related with the method that the designer have chosen to discretize the aircraft surface. The selection of  $\bar{x}$  is critical for the optimization success, several options are available: engineering like optimization variables like sweep, span, etc. or mathematical based design variables like the location of a particular control point.
- The objective function  $f(\bar{x}) : \mathbb{R}^n \rightarrow \mathbb{R}$  is the function that the designer wants to maximize or minimize. It is the element that will drive the optimization problem and should be chosen very carefully, typical options are: Minimize the drag of the aircraft or maximize its range.

- The constraints  $g_i(\bar{x}) : \mathbb{R}^n \rightarrow \mathbb{R}$ , here we specify some equalities or inequalities that the design variables should satisfy. It is important to distinguish between geometrical constraints (e.g. maximum thickness) and flow constraints (e.g. pitching moment, etc.).

The gradient based optimization in this work uses the SciPy library,<sup>24</sup> a well-established open-source software for mathematics, science and engineering. The SciPy library provides many user-friendly and efficient numerical routines for the solution of non-linear constrained optimization problems, such as conjugate gradient, Quasi-Newton or sequential least-squares programming algorithms. In particular, in this work we have used the Sequential Least Squares Programming technique.

### E. Design variable definition

Using the continuous adjoint methodology, SU2 can compute the variation of an objective function with respect to infinitesimal surface shape deformations in the direction of the local surface normal at points on the design surface. While it is possible to use each surface node in the computational mesh as a design variable capable of deformation, this approach is not often pursued in practice.

A more practical choice is to compute the surface sensitivities at each mesh node on the design surface and then to project this information into a design space made up of a smaller set (possibly a complete basis) of design variables. This procedure for computing the surface sensitivities is used repeatedly in a gradient-based optimization framework in order to march the design surface shape toward an optimum through gradient projection and mesh deformation.

In SU2 a Free-Form Deformation (FFD) strategy<sup>25,26</sup> has been adopted. Here an initial box encapsulating the object (rotor blade, wing, fuselage, etc.) to be redesigned is parameterized as a Bézier solid. A set of control points are defined on the surface of the box, the number of which depends on the order of the chosen Bernstein polynomials. The solid box is parameterized by the following expression

$$X(u, v, w) = \sum_{i=0}^l \sum_{j=0}^m \sum_{k=0}^n P_{i,j,k} B_i^l(u) B_j^m(v) B_k^n(w), \quad (25)$$

where  $l, m, n$  are the degrees of the FFD function,  $u, v, w \in [0, 1]$  are the parametric coordinates,  $P_{i,j,k}$  are the coordinates of the control point  $(i, j, k)$ , and  $B_i^l(u)$ ,  $B_j^m(v)$  and  $B_k^n(w)$  are the Bernstein polynomials. The Cartesian coordinates of the points on the surface of the object are then transformed into parametric coordinates within the Bézier box. Control points of the box become design variables, as they control the shape of the solid, and thus the shape of the surface grid inside. The box enclosing the geometry is then deformed by modifying its control points, with all the points inside the box inheriting a smooth deformation. With FFD, arbitrary changes to the thickness, sweep, twist, etc. are possible for the design of any aerospace system. Once the deformation has been applied, the new Cartesian coordinates of the object of interest can be recovered by simply evaluating the mapping inherent in Eq. 25.

## III. Redesign of the NASA Common Research Model

The NASA Common Research Model (CRM) configuration was developed to be used in CFD validation exercises as part of the fourth AIAA CFD Drag Prediction Workshop.<sup>27</sup> This is a truly open high-speed configuration with available geometry. The CRM is a low-wing, standard, tube-and-wing configuration with a flight design Mach number of 0.85. The Boeing company created the primary aerodynamic design and NASA FA (Fundamental Aerodynamics) / SFW (Subsonic Fixed Wing) held the responsibility for model design, fabrication, and testing.

The on-design condition are Mach 0.85 and a nominal lift of  $C_L = 0.5$  at Reynolds number of  $\text{Re} = 40$  million per reference chord. The reference quantities for the CRM are located in Tab. 1 where  $\lambda$  is the taper ratio and the X, Y, Z reference locations are for the main wing, not the entire vehicle. This final configuration stemmed from a 5-point optimization of the Mach number and  $C_L$  for a wing-body model with constraints on the wing thickness and spanload distribution using OVERFLOW. After the initial optimization, a nacelle/pylon component was installed to make a more realistic geometry. A horizontal tail was also designed for stability and control considerations to be robust at dive Mach number conditions with characteristics shown in Tab. 2.

Sref	594,720.0 in <sup>2</sup>
Cref	275.8 in
Span	2,313.5 in
Xref	1,325.9 in
Yref	468.75 in
Zref	177.95 in
$\lambda$	0.275
$\Lambda_{C/4}$	35°
AR	9.0

Table 1. Reference quantities for the CRM main wing.<sup>27</sup>

Sref	144,000.0 in <sup>2</sup>
Cref	184.7 in
Span	840 in
$\lambda$	0.35
$\Lambda_{C/4}$	37°

Table 2. Reference quantities for the CRM horizontal tail plane.<sup>27</sup>

### A. Validation of the Common Research Model

When redesigning a vehicle,<sup>7,28,29</sup> validation of the baseline configuration is an important component. This critical step aims to show that the available models and numerical methods that drive the optimization match the real world performance. As outlined above, the on-design condition for the CRM is Mach 0.85 and  $C_L = 0.5$ . However, for the wind tunnel tests, the Reynolds number is reduced to 5 million from 40 million both per reference chord for the on-design condition. To match these conditions, the angle of attack was changed by hand to an error tolerance of 0.001 as specified in Illi et al.<sup>30</sup> SU2 reports  $C_D = 301.3$  counts for  $C_L = 0.5$  at an angle of attack of 2.37 degrees (15M cells grid) and  $C_D = 287.8$  counts for  $C_L = 0.5$  at an angle of attack of 2.27 degrees (35M cells grid). Scalfani et al.<sup>31</sup> report  $C_D = 270.6$  counts at angle of attack of 2.364 degrees using a different mesh.

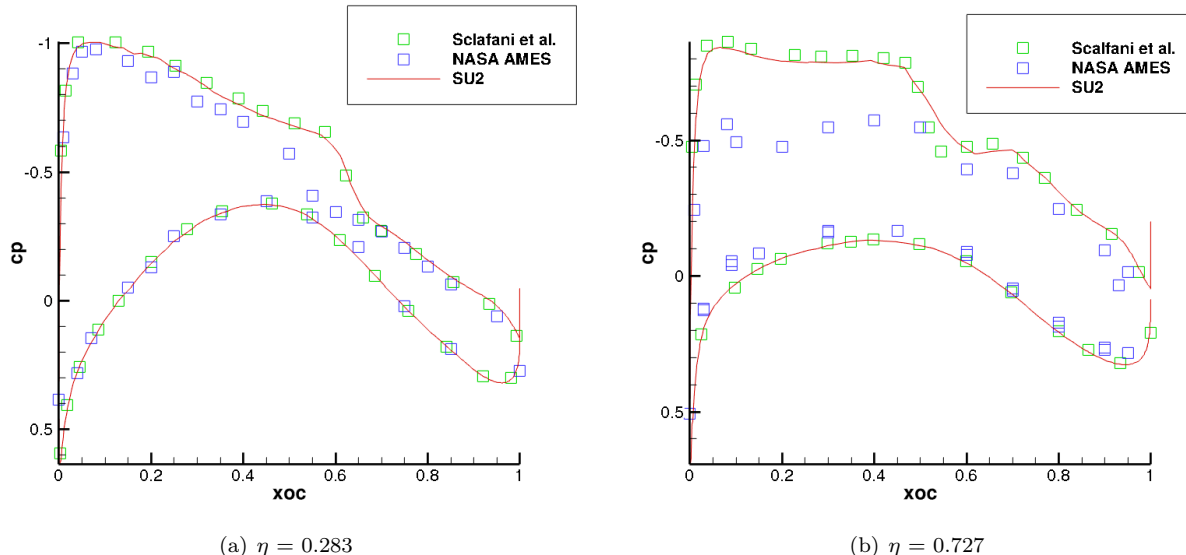


Figure 1. Comparison of SU2 (15M cells grid) at two wing stations with OVERFLOW results<sup>31</sup> and wind tunnel data.<sup>32</sup>

Beyond looking at the  $C_L$  for the configuration, pressure profiles are compared around the wing. The SU2 pressure contours at two wing stations,  $\eta = 0.283$  and  $\eta = 0.727$ , are shown in Fig. 1 along with the results of Rivers and Dittberger<sup>32</sup> and OVERFLOW results from Scalfani et al.<sup>31</sup> While neither of the CFD profiles match the wind tunnel results, the SU2 profile closely matches the OVERFLOW data except at the exact shock location on the out-board wing station. In Illi et al.,<sup>30</sup> they reference the pressure discrepancy between wind tunnel data and CFD results stems from to stronger twist in the wind tunnel experiments. Overall, there is reasonably good agreement between the available CRM data and SU2.

## B. Redesign of the Common Research Model

The present discussion summarizes a set of numerical experiments oriented toward the further optimization of a complex, previously optimized, wing-body configuration like the CRM (including the horizontal tail plane).

The design of a wing-body configuration is much more challenging than an isolated wing. In fact, a complete aircraft aerodynamic optimization requires multiple intermediate steps, the selection of the design variables has a greater impact (due to the interaction of the different aircraft components), and the problem is more likely to have multiple local minima (due to numerous constraints). In other words, in a complete aircraft redesign for aerodynamic performance, gradient-based design techniques are useful tools, but the role of the designer is still critical in driving the design to the best local optimum possible.

To present a systematic introduction to the shape redesign of the CRM configuration using gradient-based methods, we will introduce the constraints in a sequential way:

1. First, a drag minimization problem is used to check the accuracy of the gradients. At this point, it is important to note that the current methodology does not introduce the effect of the eddy viscosity in the gradient evaluation.
2. Second, a drag optimization with a  $C_L$  constraint at different angles of attack will be presented. This study provides an understanding of the bounds for the expected improvement in  $C_L$  and a qualitative estimation of the optimization effect in the geometry and pitching moment.
3. After that, and based on the previous results, the pitching moment is introduced as a constraint. In this particular optimization problem, the objective is to halve the value of the pitching moment while maintaining lift and reducing drag. It is important to note that in this exercise, we are using the X, Y, Z reference locations for the main wing.
4. Finally, a more aggressive pitching moment constraint is imposed (trimming the entire aircraft), and extra geometrical constraints (maximum thickness at different stations) are also introduced.

Size	AoA (deg)	$C_L$	$C_D$	$C_{My}$
15M cells	2.37	0.50	0.0301	-0.0442
35M cells	2.27	0.50	0.0287	-0.0475

**Table 3.** Main characteristics of the numerical grids.

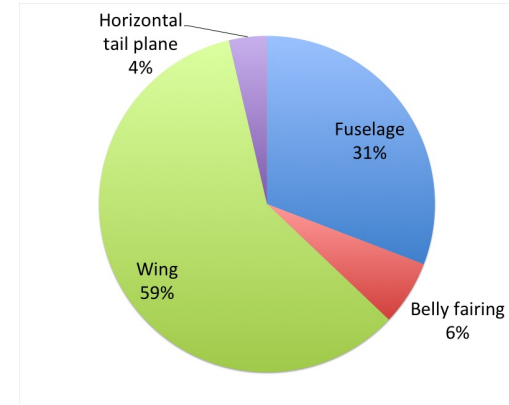


**Table 4.**  $C_D$  breakdown per components.

Throughout the redesign studies, we have used two different grids: a coarse mesh composed of 15 millions grid cells and a finer grid composed of 35 millions grid cells. The main characteristics of the numerical grids are summarized in Tab. 3 and Fig. 4. On the other hand, the location of the different wing stations that are referenced in this paper are plotted in Fig. 2 and Fig. 3.

After checking that the coarse mesh is able to reproduce the most important physical phenomena of the problem, we have used that coarse mesh as a baseline, and we will use the fine mesh to run some very specific optimization problems. At this point, it is critical to note that the continuous adjoint methodology does not require extra memory compared to the direct problem. Therefore, the motivation for selecting of the coarser numerical grid in a number of situations is purely to save computational resources and to provide a more complete paper.

As a reference, the flow solution and the adjoint sensitivities for the baseline configuration are presented in Figs. 4–7. These color maps are crucial for gaining insight into the problem and aid the designer in

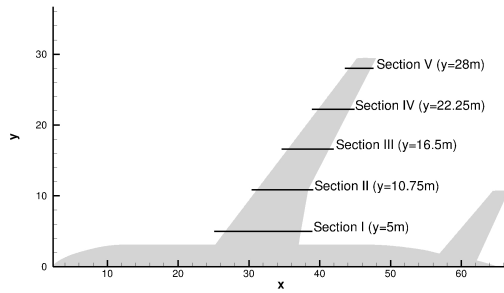


**Figure 2.** Location of the sections used to impose geometrical constraints.

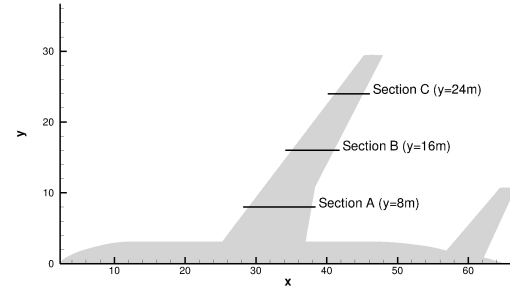


**Figure 3.** Location of the sections used to visualize the  $C_p$ .

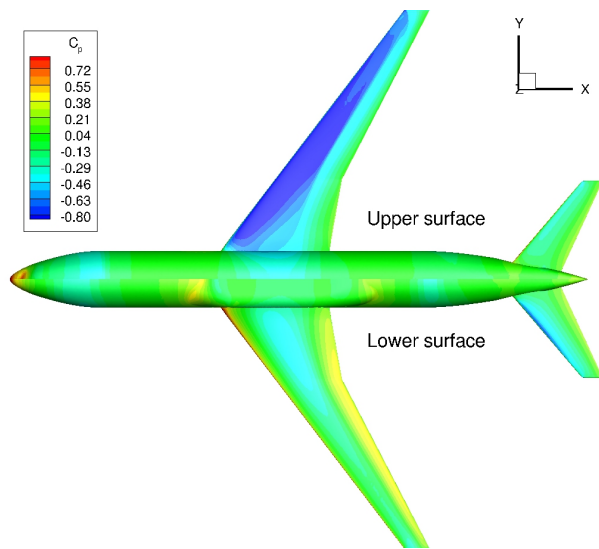


**Figure 4.**  $C_p$  contours at the upper and lower surface of the CRM configuration.

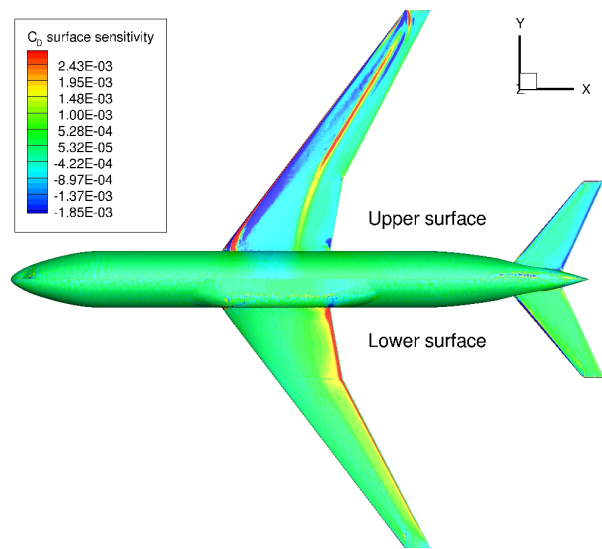


**Figure 5.**  $C_d$  sensitivity contours at the upper and lower surface of the CRM configuration.

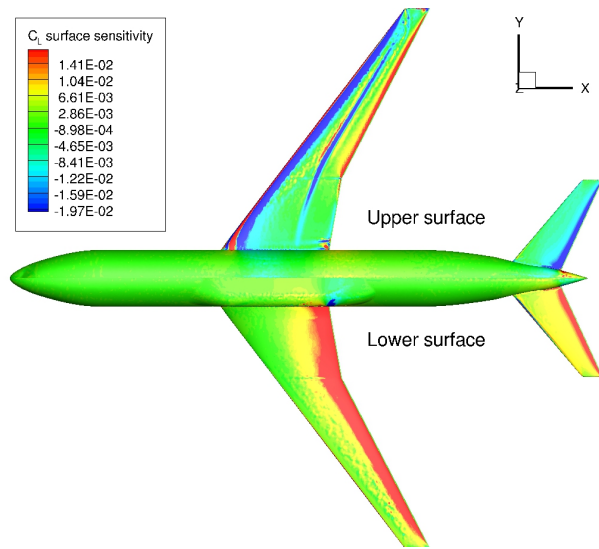


**Figure 6.**  $C_l$  sensitivity contours at the upper and lower surface of the CRM configuration.

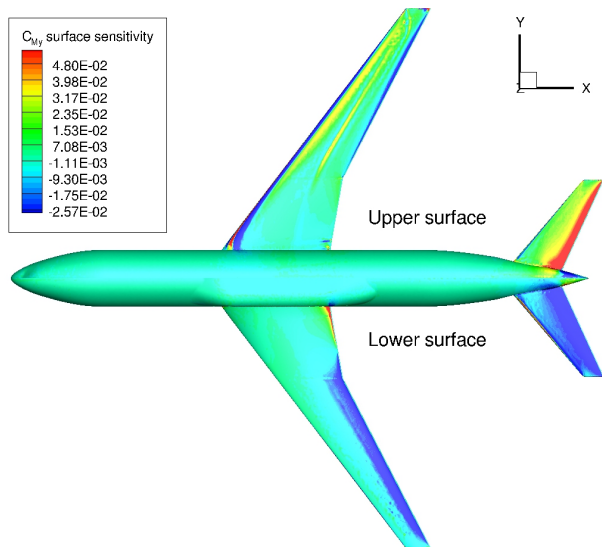


**Figure 7.**  $C_{M_y}$  sensitivity contours at the upper and lower surface of the CRM configuration.

determining the most sensitive zones of the aircraft for each functional. Additionally, this information can guide design variable selection, or in some cases, provide enough information to impose manual design changes.

### C. Selection of the design variables

During this optimization study, the kind and number of design variables have been chosen based on previous experience. In particular, 2 Free Form Deformation (FFD) boxes have been used: the first one around the main wing (see Fig. 8) features 208 control points, and the second one in the horizontal tail plane (see Fig. 9) contains 70 control points.

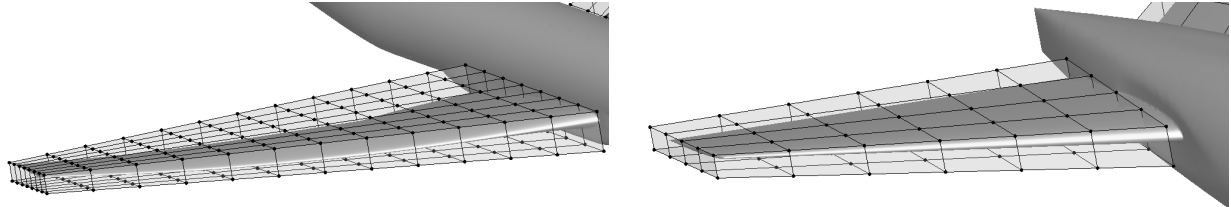


**Figure 8. FFD box at the main wing (208 control points).**

**Figure 9. FFD box at the horizontal tail plane (70 control points).**

The design variables have been defined as the movement of the FFD control points in the Z-direction and, as a geometrical constraint, we have restricted the movement of several planes of control points in order to guarantee the continuity of the first surface derivative at the root of the wing and tail. Furthermore, based on previous experience, we would like to avoid an excessive movement of the trailing edge that eventually can create unrealistic geometries. To accomplish this, an extra plane of control points have been fixed at that location. Finally, some of the optimization presented in this paper also contains specific maximum thickness constraints at different sections of the main wing (i.e., the maximum thickness of the section can not drop below 95% of the original value).

### D. Evaluation of the effect of the sharp edges sensitivities

Sharp edges (trailing edges in particular) are very challenging from the design point of view. It is well-known that these regions have a large impact on the overall lift and drag characteristics of the airplane. Moreover, they are important in a shape design setting because they represent a sensitive area that can introduce gradients that are an order of magnitude greater than those appearing across the rest of the aircraft geometry. On the other hand, from the mathematical point of view, the evaluation of the sensitivity in these non-smooth regions requires extra terms that are difficult to evaluate for complex geometries.

For that reason, SU2 features a methodology for detecting sharp edges (where a high surface sensitivity is expected) and removing that sensitivity from the gradient calculus. Obviously, the gradient without the sensitivity induced by the sharp edges remains a descent direction that is useful in any optimization algorithm.

In order to quantify the effect of the sharp edges, in Fig. 10 the drag sensitivity for each design variable is presented when the sharp edge sensitivity is used. In contrast, if we remove that sensitivity, the resulting gradient is presented in Fig. 11

We will start the evaluation of the bounded gradient with an unconstrained drag minimization. Despite the fact that this is not an interesting problem from the point of view of the overall aircraft design, it is a useful exercise to check the quality of the gradients and evaluate the effect of removing the sensitivity of the objective function at the trailing edge. In Fig. 12, the region that has been removed from the sensitivity calculus is highlighted, and in Fig. 13, the drag sensitivity is visualized (after removing the sharp edges sensitivity).

As we previously highlighted, the CRM baseline case ( $C_L=0.5$ ) has a drag of 301 counts. In order to evaluate the accuracy of the gradient, we will focus only on the first optimizer iteration or step (value of the gradient multiplied by a fixed coefficient, 50 in this particular problem). As a conclusion, if the sensitivity at the sharp edges is removed, the obtained drag is 291 counts at a  $C_L$  of 0.48. However, retaining the

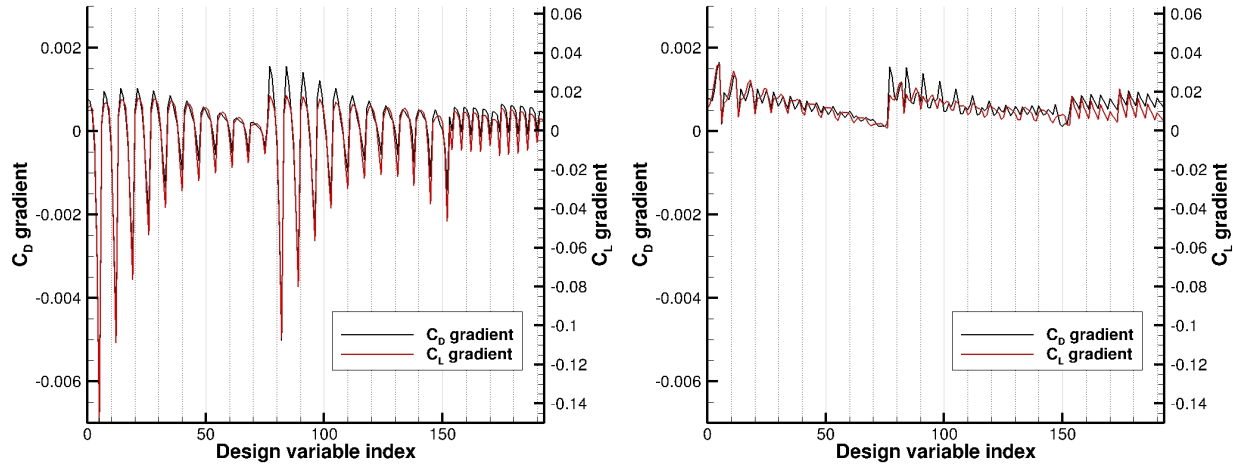


Figure 10. Drag and lift gradients including the sensitivity at the sharp edges.

Figure 11. Drag and lift gradients after removing the sensitivity at the sharp edges.

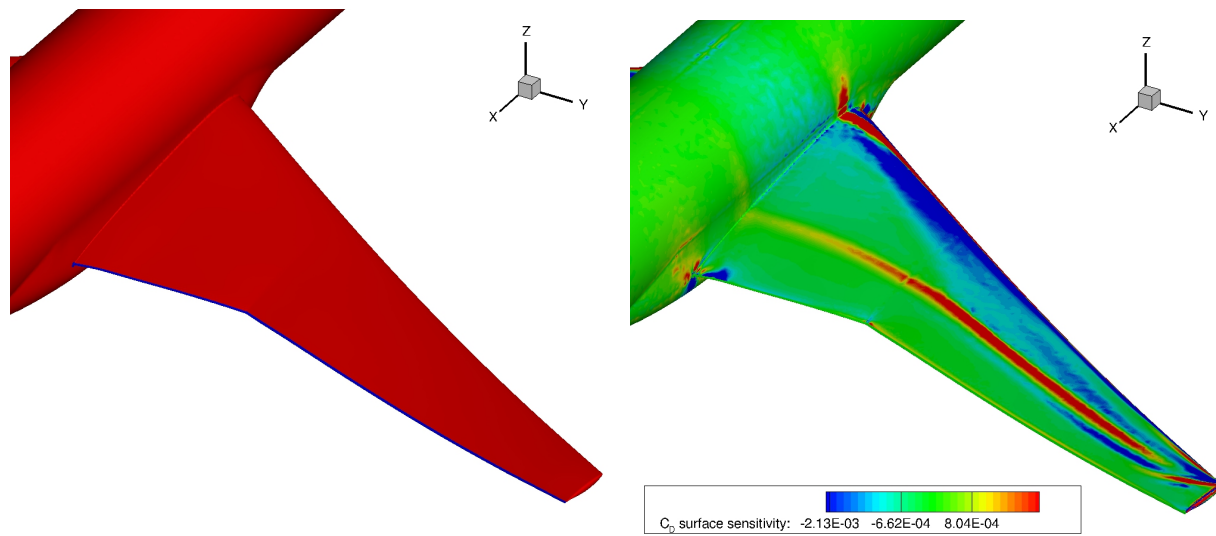


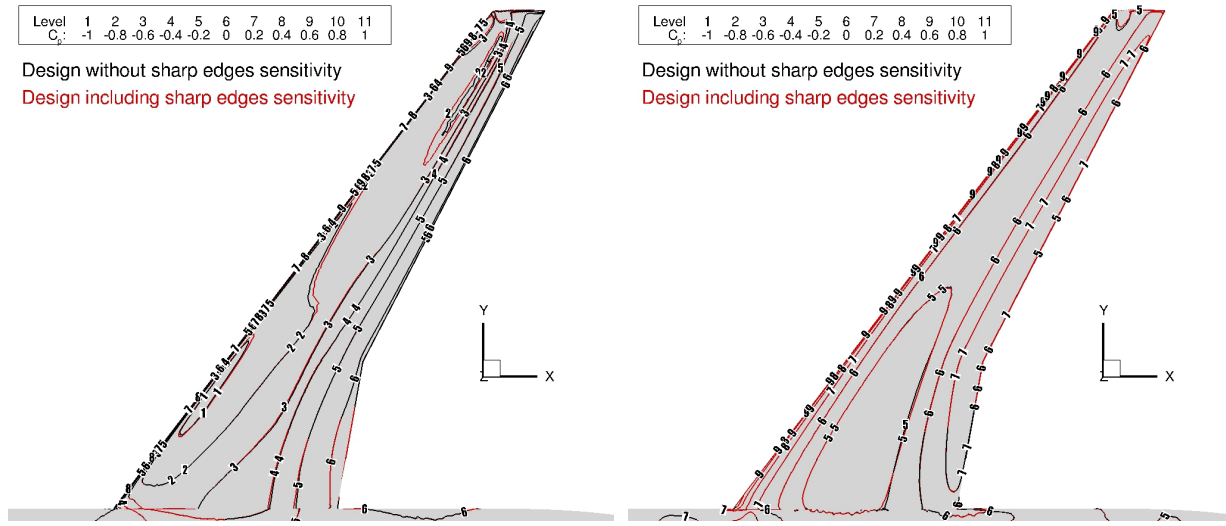
Figure 12. Region affected by the sharp edges detector, the sensitivity in the blue zone will be removed from the final calculus.

Figure 13. Drag surface sensitivity after removing the sensitivity at the sharp edges.

sensitivity at the sharp edges will reduce the drag to 263 at a  $C_L$  of 0.40. Based on these results, the sharp edge contribution seems important for obtaining the steepest descent in the gradient direction.

However, in a more practical scenario, it is important to check the combined effect of drag minimization while maintaining a baseline lift. In this optimization, if the sharp edges are active, we will obtain a drag of 297 counts with a  $C_L$  of 0.50 while, if the sensitivity at the sharp edges is removed, then we obtain 298 drag counts with a  $C_L$  of 0.5.

It is also useful to compare both designed geometries (Fig. 14 and Fig. 15) to check that, despite the clear differences in the gradient value, the final results are very similar. This leads us to conclude that the large gradient effect at the trailing edges is balanced out with a meaningful constrained optimization problem where the objective function and constraints compete. For that reason, we have decided to focus on the case without trailing edge sensitivity.



**Figure 14.** Pressure contours in the upper surface of Figure 15. **Figure 15.** Pressure contours in the lower surface of the main wing.

### E. Drag minimization, maintaining lift at different angle of attacks

We already know that the angle of attack is a critical design variable that it is not included in the set of original design variables. However, the strong effect of angle of attack can cover up the effectiveness of the shape design variables. For that reason, different optimization will be performed at different, but fixed, angles of attack.

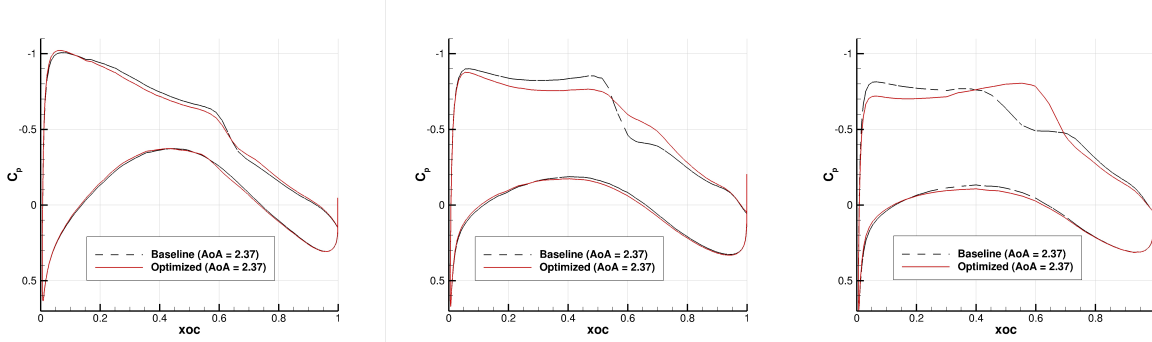


**Figure 16.** Pressure contours at Figure 17. **Figure 17.** Pressure contours at Figure 18. **Figure 18.** Pressure contours at station A  $y = 8m$  (baseline vs. de- station B  $y = 16m$  (baseline vs. de- station C  $y = 24m$  (baseline vs. de-sign, AoA = 2.37, and  $C_L = 0.50$ ). sign, AoA = 2.37, and  $C_L = 0.50$ ).

As an initial test, a free optimization problem with only a lift constraint is proposed. In particular, this experiment is repeated at three different angles of attack: 2.37deg (baseline value with  $C_L = 0.5$ ), 2.133deg (10% lower than the baseline case), and 2.607deg (10% higher than the baseline case).

We will start the discussion with the baseline case ( $\text{AoA} = 2.37\text{deg}$ ). As we noticed before, the baseline drag is 301 counts. After the optimization, it was possible to reduce the drag to 297 counts (a reduction of 4 drag counts). Despite the fact that this represents a small reduction of the total drag, the  $C_p$  sections at three different stations (see Fig. 16 to Fig. 18) depict an important change in the pressure distribution that leads to an essentially shock-free configuration. The result of this optimization problem is summarized in Tab. 5 and Tab. 6.

If the starting point is at a higher angle of attack ( $\text{AoA} = 2.607\text{deg}$ ), the final design has a drag value that is higher than the original one 306 (5 drag counts increase). However, a closer view to the  $C_p$  distribution shows that the upper surface of the wing and horizontal tail plane have clearly been optimized, and the origin of the higher drag is not on the upper wing surface but rather on the rest of the aircraft. In fact, just the increase of the angle of attack implies 23 extra drag counts, and while 18 are from the wing, the rest are mainly the increase in drag due to the fuselage.

The most interesting design is obtained if the starting point is at a lower angle of attack ( $\text{AoA} = 2.133\text{deg}$ ). At this angle of attack, the optimizer is able to recover the baseline lift at a lower drag number of 294 counts (a reduction of 7 counts). The  $C_p$  distributions for this result are shown in Figs. 19–21. The result of this optimization problem is summarized in Tab. 5 and Tab. 6.

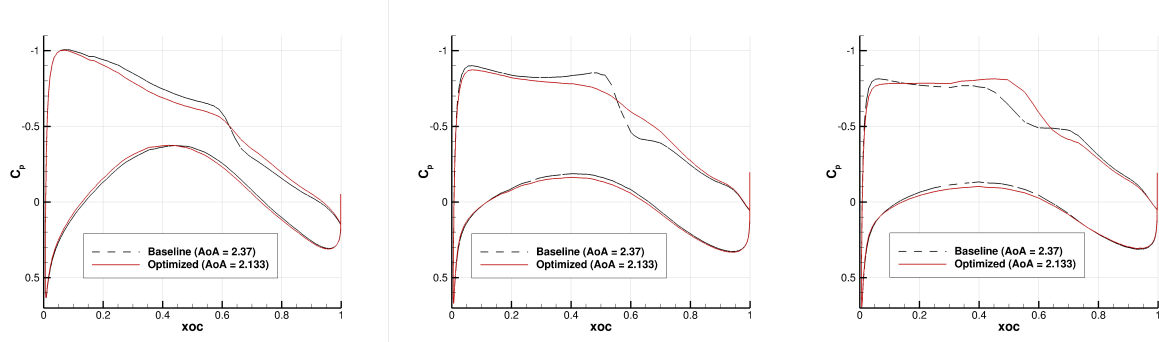


**Figure 19.** Pressure contours at station A  $y = 8\text{m}$  (baseline vs. de-sign,  $\text{AoA} = 2.133$ , and  $C_L = 0.5$ ). **Figure 20.** Pressure contours at station B  $y = 16\text{m}$  (baseline vs. de-sign,  $\text{AoA} = 2.133$ , and  $C_L = 0.5$ ). **Figure 21.** Pressure contours at station C  $y = 24\text{m}$  (baseline vs. de-sign,  $\text{AoA} = 2.133$ , and  $C_L = 0.5$ ).

Once the potential  $C_D$  reductions with a  $C_L$  constraint have been evaluated, the next step is the introduction of another flow constraint: the pitching moment  $C_{M_y}$ . It is important to emphasize that the most satisfactory design from our initial studies (drag minimization, constant lift starting with a lower angle of attack) also reduces the absolute value of the pitching moment such that aids in trimming the aircraft. Unfortunately, we also discover that the shape modifications in the main wing to minimize drag and maximize lift also increase the absolute value of the pitching moment. The horizontal tail plane, as we expect, will play a critical role in trimming the aircraft.

## F. Drag minimization, maintaining lift and decreasing pitching moment

In particular, the new objective is to halve the value of the original pitching moment, and two different starting points will be evaluated: the original angle of attack 2.37deg that produces a  $C_L$  of 0.5 and a lower angle of attack of 2.2515deg (5% of the original angle of attack), which is a compromise between the baseline lift and a reduced pitching moment to start the shape design process.

Starting with the original case (baseline  $\text{AoA} = 2.37$ ) and after a very good initial iteration, we find that the optimizer was not been able to further reduce the drag. It stalls after the second iteration. None of the test points produce a lower drag value, and the pitching moment constraint is violated. In this case, the best result corresponds with the first optimizer iteration with a  $C_D$  of 298 counts, a  $C_L$  of 0.5, and a pitching moment of -0.0346, which is a 78% of the original value -0.0441.

Starting with a slightly lower angle of attack (2.2515deg), we see that the optimization proceeds much better, and it is possible to recover the original lift of 0.5, a drag of 297 counts, and a pitching moment of

-0.0221 (50% of the original value). In this case, we have obtained a relevant reduction of 4 counts in drag with the same lift and half the pitching moment. Note that the original pitching moment at this new angle of attack was -0.0381 (86% of the original one), and the lift was 5% less than the original value. The result of this optimization problem is summarized in Tab. 5 and Tab. 6.

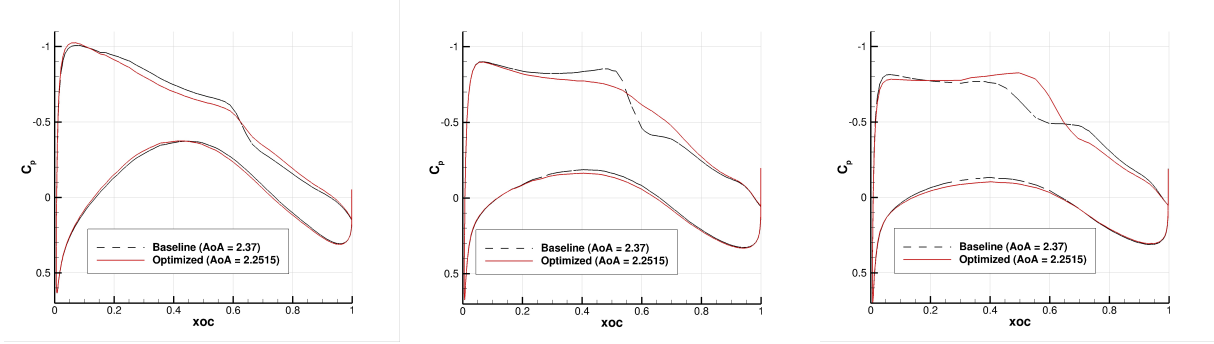


**Figure 22.** Pressure contours at station A  $y = 8m$  (baseline vs. de-sign,  $AoA = 2.2515$ ,  $C_L = 0.5$ , and sign,  $AoA = 2.2515$ ,  $C_L = 0.5$ , and  $C_{My} = -0.0221$ ). **Figure 23.** Pressure contours at station B  $y = 16m$  (baseline vs. de-sign,  $AoA = 2.37$ ,  $C_L = 0.5$ , and sign,  $AoA = 2.2515$ ,  $C_L = 0.5$ , and  $C_{My} = -0.0221$ ). **Figure 24.** Pressure contours at station C  $y = 24m$  (baseline vs. de-sign,  $AoA = 2.37$ ,  $C_L = 0.5$ , and sign,  $AoA = 2.2515$ ,  $C_L = 0.5$ , and  $C_{My} = -0.0221$ ).

The  $C_p$  distribution at different stations are summarized in Figs. 22–24. As in previous cases, it is important to note that the new configuration is shock-free, except in the most outboard sections.

As a final test, we have set a design problems that aims to trim the aircraft maintaining lift and reducing drag at a lower angle of attack ( $AoA = 2.133$ ). The history of the optimization is presented in Figs. 25–27. In these figures we also evaluate the effect of scaling the objective function and constraints in the overall optimization process. As we will describe in the next subsection, a small change in the scaling factor will produce a different final geometry.

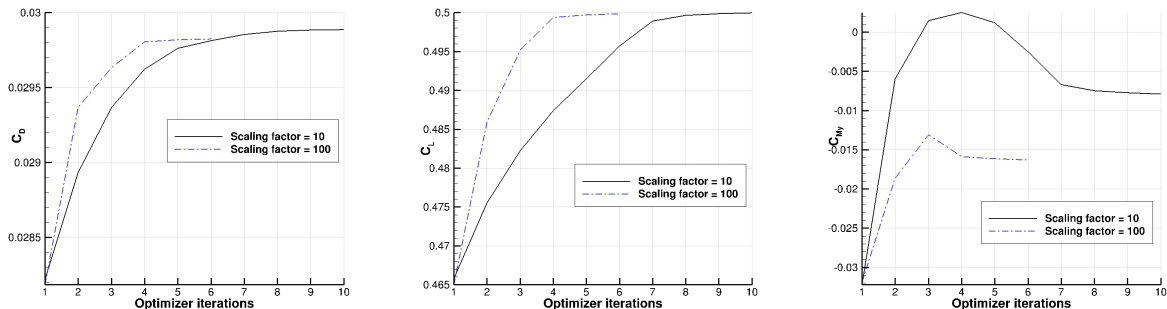


**Figure 25.**  $C_D$  optimization history, **Figure 26.**  $C_L$  optimization history, **Figure 27.**  $C_{My}$  optimization history, using different gradient and objective function scaling factors. **Figure 25.**  $C_D$  optimization history, using different gradient and objective function scaling factors. **Figure 26.**  $C_L$  optimization history, using different gradient and objective function scaling factors. **Figure 27.**  $C_{My}$  optimization history, using different gradient and objective function scaling factors.

In short, these results demonstrate that, with the current set of design variables, it is possible to trim the aircraft maintaining lift and drag (without including geometrical constraints apart from the design variable bounds). In particular, using a scaling factor of 10 the final results provides a reduction of 3 drag counts with respect to the original configuration at a pitching moment of -0.008 (18% of the original value) and maintaining lift. The result of this optimization problem is summarized in Tab. 5 and Tab. 6.

## G. Trimming the aircraft, drag minimization, and maintaining lift with maximum thickness constraints

Once we have demonstrated that it is possible to reduce the pitching moment without affecting the lift and drag of the aircraft, the next step is to completely trim the vehicle while maintaining lift and, if possible,

reduce the drag. In this particular example, the starting point is an angle of attack that is 90% of the baseline value.

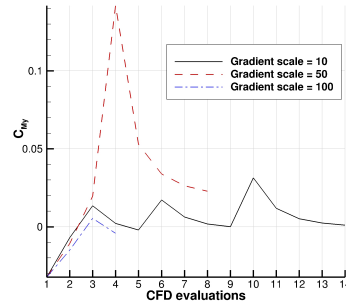
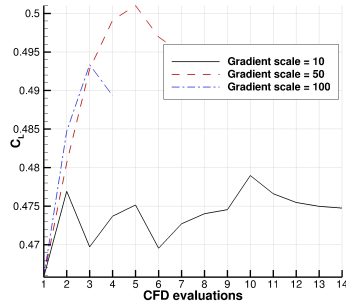
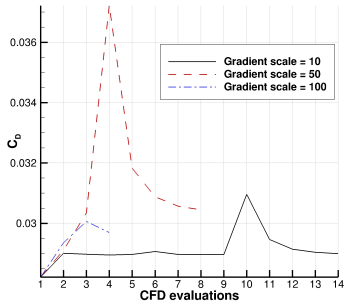


**Figure 28.**  $C_D$  optimization history, using different gradient and objective function scaling factors.

**Figure 29.**  $C_L$  optimization history, using different gradient and objective function scaling factors.

**Figure 30.**  $C_{My}$  optimization history, using different gradient and objective function scaling factors.

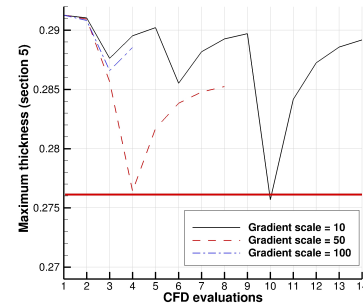
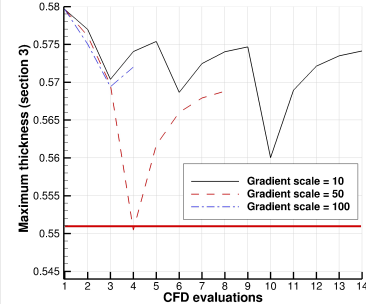
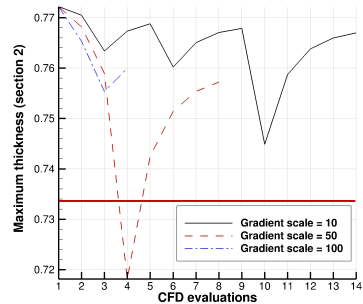


**Figure 31.** Maximum thickness at section II, using different gradient and objective function scaling factors.

**Figure 32.** Maximum thickness at section III, using different gradient and objective function scaling factors.

**Figure 33.** Maximum thickness at section V, using different gradient and objective function scaling factors.

The objective of this optimization is to emphasize the significance of the selection of the gradient scaling factor in the optimization process. In particular, from Figs. 28–33, it is possible to estimate the evolution of the lift, drag, pitching moment, and maximum thickness for the 3 different scalings of the functionals and gradients (10, 50 and 100). The optimizer behaves differently under the influence of different scaling factors.

Analyzing the results presented in Figs. 28–33, we find that there is not a solution that satisfies all of the constraints, but a scaling factor of 100 provides an acceptable point for further investigation. In particular, the obtained lift is 0.49 with 300 drag counts and a pitching moment of 0.0054, which is 12% of the original value with a 2% reduction in lift and the same drag. Note that at 2.133deg angle of attack, the pitching moment at the beginning was -0.0322, so the majority of the reduction of the pitching moment has been obtained by reshaping the wing (original pitching moment at baseline is -0.0441). The result of this optimization problem is summarized in Tab. 5 and Tab. 6.

The pressure distributions for this optimization are presented in Figs. 34–36, and the original and designed shapes are compared in Figs. 37–38. In this particular problem, geometrical constraints (maintaining 95% of the baseline maximum thickness) at different section have been satisfied.

In conclusion, it is important to highlight that in this final optimization, we have really just scratched the surface of problem. Gradient-based techniques are very important, powerful tools for treating the present type of shape design problem in aeronautics, and yet, the choices related to the right combination/scaling of the design variables (wing, tail, and angle of attack) and constraints are fundamental in order to obtain fully satisfactory solutions. Given the current optimizer technology, the intuition, experience, and decision-making ability of the designer remain critical in this type of complex, industrial design process.

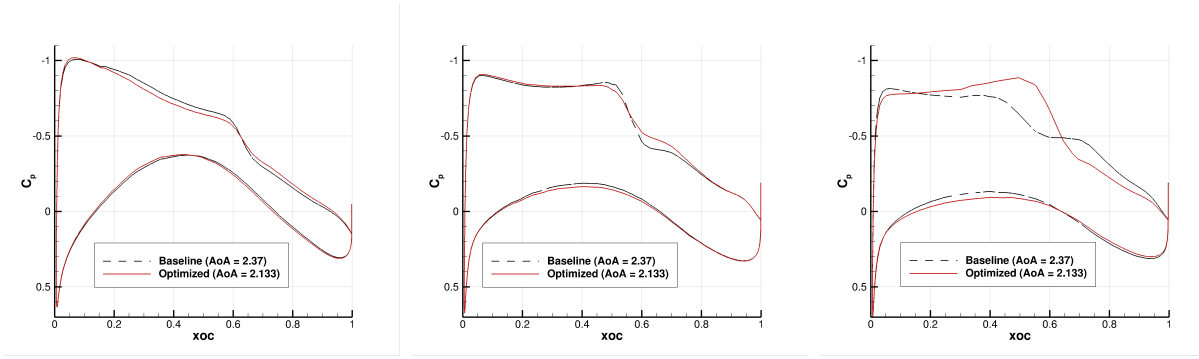


**Figure 34.** Pressure contours at **Figure 35.** Pressure contours at **Figure 36.** Pressure contours at station A  $y = 8m$  (baseline vs. de- station B  $y = 16m$  (baseline vs. de- station C  $y = 24m$  (baseline vs. design,  $AoA = 2.133$ ,  $C_L = 0.5$ , and sign,  $AoA = 2.133$ ,  $C_L = 0.5$ , and sign,  $AoA = 2.133$ ,  $C_L = 0.5$ , and  $CM_y = 0.0054$ ).

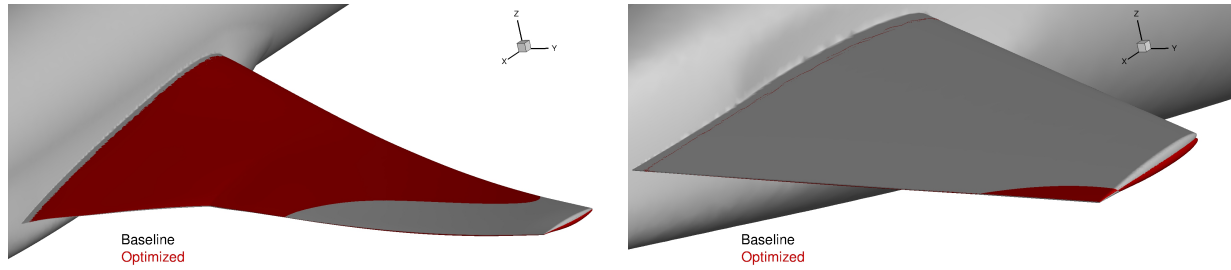


**Figure 37.** Shape comparison baseline vs. design at **Figure 38.** Shape comparison baseline vs. design at the main wing. the horizontal tail plane.

Design problem	$C_L$					$C_D$				
	Total	Fuselage	Fairing	Wing	Tail	Total	Fuselage	Fairing	Wing	Tail
Baseline at $AoA=2.37$	0.50	0.07	-0.01	0.46	-0.02	301.3	92.9	18.8	178.5	11.0
Min $C_D$ , $C_L = 0.5$ at $AoA=2.37$	0.50	0.07	-0.01	0.46	-0.02	297.7	92.8	18.7	175.8	10.4
Min $C_D$ , $C_L = 0.5$ at $AoA=2.133$	0.50	0.07	-0.01	0.46	-0.02	294.1	89.8	18.6	174.6	11.0
Min $C_D$ , $C_L = 0.5$ , $C_M > -0.022$ at $AoA=2.2515$	0.50	0.07	-0.01	0.47	-0.03	297.6	91.4	18.7	178.4	9.0
Min $C_D$ , $C_L = 0.5$ , $C_M > 0.0$ , at $AoA=2.133$	0.50	0.07	-0.01	0.47	-0.03	298.9	90.2	18.7	181.6	8.3
Min $C_D$ , $C_L = 0.5$ , $C_M > 0.0$ , MaxThickness > 95% at $AoA=2.133$	0.49	0.07	-0.01	0.47	-0.03	300.6	90.2	18.8	183.6	8.1

**Table 5.** Summary of the different optimizations ( $C_L$  and  $C_D$ ).

Design	$C_{My}$				
	Total	Fuselage	Fairing	Wing	Tail
Baseline at AoA=2.37	-0.044	0.046	0.002	-0.158	0.066
Min $C_D$ , $C_L = 0.5$ at AoA=2.37	-0.045	0.047	0.002	-0.170	0.076
Min $C_D$ , $C_L = 0.5$ at AoA=2.133	-0.059	0.043	0.001	-0.174	0.071
Min $C_D$ , $C_L = 0.5$ , $C_M > -0.022$ at AoA=2.2515	-0.022	0.046	0.002	-0.174	0.104
Min $C_D$ , $C_L = 0.5$ , $C_M > 0.0$ , at AoA=2.133	-0.008	0.044	0.001	-0.177	0.123
Min $C_D$ , $C_L = 0.5$ , $C_M > 0.0$ , MaxThickness > 95% at AoA=2.133	0.005	0.046	0.002	-0.171	0.129

Table 6. Summary of the different optimizations ( $C_{My}$ ).

## IV. Conclusions

This article has successfully demonstrated the use of the continuous adjoint methodology in the SU2 suite for large-scale aerodynamic shape design with a realistic aircraft configuration, the NASA CRM, and unstructured meshes. The continuous adjoint methodology was detailed and then applied to a wide range of optimization problems aimed at reducing the drag of the aircraft while imposing various constraints on geometry (wing thicknesses), lift, and moments. In each scenario, the redesign produced meaningful improvements in performance while satisfying constraints.

This type of continuous adjoint methodology exhibits a number of the qualities that we desire when attempting large-scale shape design. In particular, obtaining a surface formulation for shape design gradients, the ability to tailor numerical solution methods for the adjoint equations (to help mitigate numerical stiffness), and low overhead in terms of compute and memory (since much of the same code infrastructure and numerical methods can be reused from the primal problem) make the continuous adjoint approach particularly attractive. The successful demonstration of the methodology at large-scale coupled with the above qualities reinforce the tremendous potential for the application of continuous adjoints to realistic problems of industrial interest.

## V. Acknowledgements

The authors would like to acknowledge the generous support from the Intel Software & Services Group (SSG) Developer Relations Division (DRD), including access to Intel Corporation's Endeavour high-performance computing cluster in Rio Rancho, New Mexico, without which this paper would not have been possible.

## Appendix

In this appendix we give the main formulas required to compute the sensitivities discussed above.

### A. Navier-Stokes equations

As usual in the Navier-Stokes equations, system (1) considers separately the convective terms, denoted by  $\vec{F}_i^c$ , and the viscous ones, denoted here by  $\vec{F}_i^{v1}$  and  $\vec{F}_i^{v2}$ . They are given by

$$\vec{F}_i^c = \begin{pmatrix} \rho v_i \\ \rho v_i v_1 + P \delta_{i1} \\ \rho v_i v_2 + P \delta_{i2} \\ \rho v_i v_3 + P \delta_{i3} \\ \rho v_i H \end{pmatrix}, \quad \vec{F}_i^{v1} = \begin{pmatrix} \cdot \\ \tau_{i1} \\ \tau_{i2} \\ \tau_{i3} \\ v_j \tau_{ij} \end{pmatrix}, \quad \vec{F}_i^{v2} = \begin{pmatrix} \cdot \\ \cdot \\ \cdot \\ \cdot \\ C_p \partial_i T \end{pmatrix}, \quad i = 1, \dots, 3 \quad (26)$$

where  $v_i$  are the Cartesian velocity components,  $H$  is the fluid enthalpy,  $\delta_{ij}$  is the Kronecker delta function, and  $\tau_{ij} = \partial_j v_i + \partial_i v_j - \frac{2}{3} \delta_{ij} \nabla \cdot \vec{v}$ . Recall that latin indexes  $i, j$  denote 3D Cartesian coordinates, with repeated

indexes implying summation. In these formulas,  $C_p$  is the specific heat at constant pressure,  $T = \frac{P}{R\rho}$  is the temperature, and  $R$  is the gas constant, so that for an ideal gas  $\frac{C_p}{R} = \frac{\gamma}{(\gamma-1)}$ , with  $\gamma$  constant. In order to close the system, the dynamic viscosity is assumed to satisfy the Sutherland's law,  $\mu_{dyn} = \frac{\mu_1 T^{3/2}}{T + \mu_2}$ , where  $\mu_1$  and  $\mu_2$  are also specified constants.

## B. Linearized Navier-Stokes equations

In this section we compute  $\frac{\partial R_U}{\partial U} \delta U$  in (12).

$$\frac{\partial R_U}{\partial U} \delta U = \nabla(\vec{A}^c \delta U) - \nabla \cdot \left( \vec{F}^{vk} \frac{\partial \mu_{tot}^k}{\partial U} \delta U + \mu_{tot}^k \vec{A}^{vk} \delta U + \mu_{tot}^k \mathbf{D}^{vk} \nabla \delta U \right) \quad (27)$$

where

$$\frac{\partial \mu_{tot}^1}{\partial U} = \frac{\partial \mu_{dyn}}{\partial U} + \frac{\partial \mu_{tur}}{\partial U}, \quad \frac{\partial \mu_{tot}^2}{\partial U} = \frac{1}{Pr_d} \frac{\partial \mu_{dyn}}{\partial U} + \frac{1}{Pr_t} \frac{\partial \mu_{tur}}{\partial U}$$

and

$$\frac{\partial \mu_{dyn}}{\partial U} = \frac{\partial \mu_{dyn}}{\partial T} \frac{\partial T}{\partial U}, \quad \frac{\partial \mu_{dyn}}{\partial T} = \mu_{dyn} \frac{T + 3\mu_2}{2T(T + \mu_2)} \quad (28)$$

(29)

with  $\frac{\partial T}{\partial U} = \frac{(\gamma-1)}{R\rho} (|\vec{v}|^2 - E, -v_1, -v_2, -v_3, 1)$  and  $\frac{\partial \rho}{\partial U} = (1, 0, 0, 0, 0)$ .  
In (27) we have

$$\left. \begin{aligned} \vec{A}^c &= (A_x^c, A_y^c, A_z^c), & A_i^c &= \left. \frac{\partial \vec{F}_i^c}{\partial U} \right|_{U(x,y,z)} \\ \vec{A}^{vk} &= (A_x^{vk}, A_y^{vk}, A_z^{vk}), & A_i^{vk} &= \left. \frac{\partial \vec{F}_i^{vk}}{\partial U} \right|_{U(x,y,z)} \\ \mathbf{D}^{vk} &= \begin{pmatrix} D_{xx}^{vk} & D_{xy}^{vk} & D_{xz}^{vk} \\ D_{yx}^{vk} & D_{yy}^{vk} & D_{yz}^{vk} \\ D_{zx}^{vk} & D_{zy}^{vk} & D_{zz}^{vk} \end{pmatrix}, & D_{ij}^{vk} &= \left. \frac{\partial \vec{F}_i^{vk}}{\partial (\partial_j U)} \right|_{U(x,y,z)} \end{aligned} \right\} \quad i, j = 1 \dots 3, \quad k = 1, 2 \quad (29)$$

Defining for convenience  $a_0 = (\gamma - 1)$ ,  $\phi = (\gamma - 1) \frac{|\vec{v}|^2}{2}$ , then we have

$$\begin{aligned} A_i^c &= \begin{pmatrix} \cdot & \delta_{i1} & \delta_{i2} & \delta_{i3} & \cdot \\ -v_i v_1 + \delta_{i1} \phi & v_i - (a_0 - 1) v_i \delta_{i1} & v_1 \delta_{i2} - a_0 v_2 \delta_{i1} & v_1 \delta_{i3} - a_0 v_3 \delta_{i1} & a_0 \delta_{i1} \\ -v_i v_2 + \delta_{i2} \phi & v_2 \delta_{i1} - a_0 v_1 \delta_{i2} & v_i - (a_0 - 1) v_i \delta_{i2} & v_2 \delta_{i3} - a_0 v_3 \delta_{i2} & a_0 \delta_{i2} \\ -v_i v_3 + \delta_{i3} \phi & v_3 \delta_{i1} - a_0 v_1 \delta_{i3} & v_3 \delta_{i2} - a_0 v_2 \delta_{i3} & v_i - (a_0 - 1) v_i \delta_{i3} & a_0 \delta_{i3} \\ v_i (\phi - H) & -a_0 v_i v_1 + H \delta_{i1} & -a_0 v_i v_2 + H \delta_{i2} & -a_0 v_i v_3 + H \delta_{i3} & \gamma v_i \end{pmatrix} \\ A_i^{v1} &= \begin{pmatrix} \cdot & \cdot & \cdot & \cdot & \cdot \\ -\eta_{i1} & \partial_i \left( \frac{1}{\rho} \right) + \frac{1}{3} \partial_1 \left( \frac{1}{\rho} \right) \delta_{i1} & \partial_1 \left( \frac{1}{\rho} \right) \delta_{i2} - \frac{2}{3} \partial_2 \left( \frac{1}{\rho} \right) \delta_{i1} & \partial_1 \left( \frac{1}{\rho} \right) \delta_{i3} - \frac{2}{3} \partial_3 \left( \frac{1}{\rho} \right) \delta_{i1} & \cdot \\ -\eta_{i2} & \partial_2 \left( \frac{1}{\rho} \right) \delta_{i1} - \frac{2}{3} \partial_1 \left( \frac{1}{\rho} \right) \delta_{i2} & \partial_i \left( \frac{1}{\rho} \right) + \frac{1}{3} \partial_2 \left( \frac{1}{\rho} \right) \delta_{i2} & \partial_2 \left( \frac{1}{\rho} \right) \delta_{i3} - \frac{2}{3} \partial_3 \left( \frac{1}{\rho} \right) \delta_{i2} & \cdot \\ -\eta_{i3} & \partial_3 \left( \frac{1}{\rho} \right) \delta_{i1} - \frac{2}{3} \partial_1 \left( \frac{1}{\rho} \right) \delta_{i3} & \partial_3 \left( \frac{1}{\rho} \right) \delta_{i2} - \frac{2}{3} \partial_2 \left( \frac{1}{\rho} \right) \delta_{i3} & \partial_i \left( \frac{1}{\rho} \right) + \frac{1}{3} \partial_3 \left( \frac{1}{\rho} \right) \delta_{i3} & \cdot \\ v_j \pi_{ij} & v_j \partial_j \left( \frac{1}{\rho} \right) \delta_{i1} + \zeta_{i1} + \frac{1}{\rho} \tau_{i1} & v_j \partial_j \left( \frac{1}{\rho} \right) \delta_{i2} + \zeta_{i2} + \frac{1}{\rho} \tau_{i2} & v_j \partial_j \left( \frac{1}{\rho} \right) \delta_{i3} + \zeta_{i3} + \frac{1}{\rho} \tau_{i3} & \cdot \end{pmatrix} \\ A_i^{v2} &= \gamma \begin{pmatrix} \cdot & \cdot & \cdot & \cdot & \cdot \\ \cdot & \cdot & \cdot & \cdot & \cdot \\ \cdot & \cdot & \cdot & \cdot & \cdot \\ \cdot & \cdot & \cdot & \cdot & \cdot \\ \frac{1}{a_0} \partial_i \left( \frac{\phi}{\rho} - \frac{P}{\rho^2} \right) & -\partial_i \left( \frac{v_1}{\rho} \right) & -\partial_i \left( \frac{v_2}{\rho} \right) & -\partial_i \left( \frac{v_3}{\rho} \right) & \partial_i \left( \frac{1}{\rho} \right) \end{pmatrix} \end{aligned}$$

$$\begin{aligned}
D_{ii}^{v1} &= \frac{1}{\rho} \begin{pmatrix} \cdot & \cdot & \cdot & \cdot & \cdot \\ -\left(1 + \frac{1}{3}\delta_{i1}\right)v_1 & \left(1 + \frac{1}{3}\delta_{i1}\right) & \cdot & \cdot & \cdot \\ -\left(1 + \frac{1}{3}\delta_{i2}\right)v_2 & \cdot & \left(1 + \frac{1}{3}\delta_{i2}\right) & \cdot & \cdot \\ -\left(1 + \frac{1}{3}\delta_{i3}\right)v_3 & \cdot & \cdot & \left(1 + \frac{1}{3}\delta_{i3}\right) & \cdot \\ -|\vec{v}|^2 - \frac{1}{3}v_i^2 & \left(1 + \frac{1}{3}\delta_{i1}\right)v_1 & \left(1 + \frac{1}{3}\delta_{i2}\right)v_2 & \left(1 + \frac{1}{3}\delta_{i3}\right)v_3 & \cdot \end{pmatrix} \\
D_{ij}^{v1} &= \frac{1}{\rho} \begin{pmatrix} \cdot & \cdot & \cdot & \cdot & \cdot \\ -v_i\delta_{j1} + \frac{2}{3}v_j\delta_{i1} & \delta_{j1}\delta_{i1} - \frac{2}{3}\delta_{i1}\delta_{j1} & \delta_{j1}\delta_{i2} - \frac{2}{3}\delta_{i1}\delta_{j2} & \delta_{j1}\delta_{i3} - \frac{2}{3}\delta_{i1}\delta_{j3} & \cdot \\ -v_i\delta_{j2} + \frac{2}{3}v_j\delta_{i2} & \delta_{j2}\delta_{i1} - \frac{2}{3}\delta_{i2}\delta_{j1} & \delta_{j2}\delta_{i2} - \frac{2}{3}\delta_{i2}\delta_{j2} & \delta_{j2}\delta_{i3} - \frac{2}{3}\delta_{i2}\delta_{j3} & \cdot \\ -v_i\delta_{j3} + \frac{2}{3}v_j\delta_{i3} & \delta_{j3}\delta_{i1} - \frac{2}{3}\delta_{i3}\delta_{j1} & \delta_{j3}\delta_{i2} - \frac{2}{3}\delta_{i3}\delta_{j2} & \delta_{j3}\delta_{i3} - \frac{2}{3}\delta_{i3}\delta_{j3} & \cdot \\ -\frac{1}{3}v_i v_j & v_j\delta_{i1} - \frac{2}{3}v_i\delta_{j1} & v_j\delta_{i2} - \frac{2}{3}v_i\delta_{j2} & v_j\delta_{i3} - \frac{2}{3}v_i\delta_{j3} & \cdot \end{pmatrix} \quad (i \neq j) \\
D_{ii}^{v2} &= \frac{\gamma}{\rho} \begin{pmatrix} \cdot & \cdot & \cdot & \cdot & \cdot \\ \cdot & \cdot & \cdot & \cdot & \cdot \\ \cdot & \cdot & \cdot & \cdot & \cdot \\ \cdot & \cdot & \cdot & \cdot & \cdot \\ \frac{1}{a_0} \left(\phi - \frac{P}{\rho}\right) & -v_1 & -v_2 & -v_3 & 1 \end{pmatrix} \\
D_{ij}^{v2} &= \mathbf{0}_{5 \times 5} \quad (i \neq j)
\end{aligned}$$

where tensors  $\bar{\eta}$ ,  $\bar{\pi}$  and  $\bar{\zeta}$  in the definition of  $A_i^{v1}$  are given by

$$\begin{aligned}
\eta_{ij} &= \partial_i \left( \frac{v_j}{\rho} \right) + \partial_j \left( \frac{v_i}{\rho} \right) - \frac{2}{3} \delta_{ij} \nabla \cdot \left( \frac{\vec{v}}{\rho} \right) \\
\pi_{ij} &= v_j \partial_i \left( \frac{1}{\rho} \right) + v_i \partial_j \left( \frac{1}{\rho} \right) - \frac{2}{3} \delta_{ij} \vec{v} \cdot \nabla \left( \frac{1}{\rho} \right) = \eta_{ij} - \frac{1}{\rho} \tau_{ij} \\
\zeta_{ij} &= v_j \partial_i \left( \frac{1}{\rho} \right) - v_i \partial_j \left( \frac{1}{\rho} \right) + \frac{1}{3} v_i \partial_j \left( \frac{1}{\rho} \right).
\end{aligned}$$

### C. Adjoint formulas

In this section we give explicit formulas for the adjoint operators and boundary conditions. These are obtained from the identity (13), which is deduced from the following integration by parts

$$\int_{\Omega} \Psi_U^T \left( \frac{\partial R_U}{\partial U} \delta U \right) = \int_{\Omega} (A_U \Psi_U)^T \delta U - \int_S \vec{\varphi} \cdot (\delta P \vec{n} - \delta \bar{\sigma} \cdot \vec{n}) - \int_S (\vec{g}_1 \cdot \vec{\varphi} + g_2 \partial_n \psi_5) \delta T - \int_S \hat{g} \delta S \quad (26)$$

where we have used  $\partial_n d_S = -1$ . Here, domain integrals on the right hand side contain the adjoint operators, given by

$$A_U \Psi_U = -\nabla \Psi_U^T \cdot \vec{A}^c - \nabla \cdot (\nabla \Psi_U^T \cdot \mu_{tot}^k \mathbf{D}^{vk}) + \nabla \Psi_U^T \cdot \mu_{tot}^k \vec{A}^{vk} + \nabla \Psi_U^T \cdot \vec{F}^{vk} \frac{\partial \mu_{tot}^k}{\partial U}. \quad (27)$$

The terms  $\vec{g}_1$ ,  $g_2$  and  $\hat{g}$  appearing in the boundary integrals in (C) are given by

$$\vec{g}_1 = \frac{\partial \mu_{dyn}}{\partial T} \vec{n} \cdot \bar{\sigma}, \quad g_2 = C_p \mu_{tot}^2 \quad (28)$$

$$\begin{aligned}
\hat{g} &= -(\rho \psi_1 + \rho H \psi_5) (\partial_n \vec{v} \cdot \vec{n}) + \psi_5 \vec{n} \cdot \bar{\sigma} \cdot \partial_n \vec{v} - \vec{n} \cdot \bar{\Sigma}^{\varphi} \cdot \partial_n \vec{v} \\
&\quad - \psi_5 \bar{\sigma} : \nabla \vec{v} + \mu_{tot}^2 C_p \nabla_S \psi_5 \cdot \nabla_S T
\end{aligned} \quad (28)$$

where  $\bar{\sigma} : \nabla \vec{v} = \sigma_{ij} \partial_i v_j$ , with

$$\bar{\Sigma}^{\varphi} = \mu_{tot}^1 \left( \nabla \vec{\varphi} + \nabla \vec{\varphi}^T - \mathbf{I}_d \frac{2}{3} \nabla \cdot \vec{\varphi} \right).$$

Some of the terms in  $\hat{g}$  above can be simplified. In particular, taking into account that  $\vec{v} = 0$  and  $\nabla_S \vec{v} = 0$  on the obstacle surface, we have  $\nabla \vec{v} = \partial_j v_i = \partial_n v_i n_j$ . Therefore

$$\bar{\sigma} : \nabla \vec{v} = \sigma_{ij} \partial_n v_i n_j = \vec{n} \cdot \bar{\sigma} \cdot \partial_n \vec{v} \quad \text{on } S,$$

and the second and fourth terms in (28) cancel. On the other hand, the continuity equation yields  $\nabla \cdot \vec{v} = 0$  on  $S$ . Hence

$$0 = \nabla \cdot \vec{v} = \partial_i v_i = \partial_n v_i n_i = \partial_n \vec{v} \cdot \vec{n} \quad \text{on } S,$$

and the first term in (28) also cancels. Thus, the term  $\hat{g}$  reads

$$\hat{g} = -\vec{n} \cdot \bar{\Sigma}^\varphi \cdot \partial_n \vec{v} + \mu_{tot}^2 C_p \nabla_S \psi_5 \cdot \nabla_S T. \quad (28)$$

## References

- <sup>1</sup>A. Jameson. The present status, challenges, and future developments in computational fluid dynamics. In AGARD, editor, *Progress and challenges in CFD methods and algorithms*, 1995.
- <sup>2</sup>A. Jameson. Aerodynamic design via control theory. *Journal of Scientific Computing*, 3:233–260, 1988.
- <sup>3</sup>A. Jameson. Computational aerodynamics for aircraft design. *Science*, 245(4916):361–371, 1989.
- <sup>4</sup>A. Jameson. Optimum aerodynamic design using CFD and control theory. *AIAA Paper 95-1729*, 1995.
- <sup>5</sup>A. Jameson, N. A. Pierce, and L. Martinelli. Optimum aerodynamic design using the Navier-Stokes equations. *Theoretical and Computational Fluid Dynamics*, 10:213–237, 1998.
- <sup>6</sup>A. Jameson, J. J. Alonso, J. Reuther, L. Martinelli, and J.C. Vassberg. Aerodynamic shape optimization techniques based on control theory. *AIAA Paper 1998-2538*, 29th Fluid Dynamics Conference, Albuquerque, NM, June 1998.
- <sup>7</sup>J. Vassberg and A. Jameson. Aerodynamic shape optimization part ii: Sample applications. In *Lecture Notes Presented at the VKI Lecture Series*, Rhode Saint Genese Begium, 2 2006. Von karman Institute for fluid dynamics.
- <sup>8</sup>W. K. Anderson and V. Venkatakrishnan. Aerodynamic design optimization on unstructured grids with a continuous adjoint formulation. *AIAA Paper 1997-0643*, 1997.
- <sup>9</sup>A. Jameson and S. Kim. Reduction of the adjoint gradient formula for aerodynamic shape optimization problems. *AIAA Journal*, 41(11):2114–2129, 2003.
- <sup>10</sup>C. Castro, C. Lozano, F. Palacios, and E. Zuazua. A systematic continuous adjoint approach to viscous aerodynamic design on unstructured grids. *AIAA Journal*, 45(9):2125–2139, 2007.
- <sup>11</sup>J. Sokolowski and J.-P. Zolesio. *Introduction to shape optimization*. Springer Verlag, New York, 1991.
- <sup>12</sup>S. Ta'asan. Introduction to shape design and control. In *VKI Lecture Series*, Rhode Saint Genese Begium, 1997. Von karman Institute for fluid dynamics.
- <sup>13</sup>F. Palacios, J. J. Alonso, M. Colombo, J. Hicken, and T. Lukaczyk. Adjoint-based method for supersonic aircraft design using equivalent area distributions. *AIAA Paper 2012-0269*, 2012.
- <sup>14</sup>S. Schmidt, V. Schulz, C. Ilic, and N. R. Gauger. Three-dimensional large-scale aerodynamic design based on shape calculus. *AIAA Journal*, 51(11), November 2013.
- <sup>15</sup>A. Bueno-Orovio, C. Castro, F. Palacios, and E. Zuazua. Continuous adjoint approach for the Spalart–Allmaras model in aerodynamic optimization. *AIAA Journal*, 50(3), 2012.
- <sup>16</sup>F.M. White. *Viscous Fluid Flow*. McGraw Hill Inc., New York, 1974.
- <sup>17</sup>L.D. Landau and E.M. Lifshitz. *Fluid Mechanics (2nd Edition)*. Pergamon Press, 1993.
- <sup>18</sup>D.C. Wilcox. *Turbulence Modeling for CFD*. 2nd Ed., DCW Industries, Inc., 1998.
- <sup>19</sup>O. Pironneau. *Finite element methods for fluids*. John Wiley and Sons, Inc., New York, 1990.
- <sup>20</sup>C. Castro, C. Lozano, F. Palacios, and E. Zuazua. A systematic continuous adjoint approach to viscous aerodynamic design on unstructured grids. *AIAA Journal*, 45(9):2125–2139, 2007. DOI: 10.2514/1.24859.
- <sup>21</sup>T. D. Economou, F. Palacios, and J. J. Alonso. A viscous continuous adjoint approach for the design of rotating engineering applications. *AIAA Paper 2013-2580*, June 2013.
- <sup>22</sup>J. Sokolowski and J.-P. Zolesio. *Introduction to shape optimization*. Springer Verlag, New York, 1991.
- <sup>23</sup>A. Baeza, C. Castro, F. Palacios, and E. Zuazua. 2-D Euler shape design on nonregular flows using adjoint Rankine-Hugoniot relations. *AIAA Journal*, 47 (3):552–562, 2009. DOI: 10.2514/1.37149.
- <sup>24</sup>E. Jones, T. Oliphant, P. Peterson, et al. SciPy: Open source scientific tools for Python, 2001–.
- <sup>25</sup>T. W. Sederberg and S. R. Parry. Free-form deformation of solid geometric models. *Proceedings of SIGGRAPH 89 (Computer Graphics)*, 20(4):151–159, 1986.
- <sup>26</sup>J. A. Samareh. Aerodynamic shape optimization based on free-form deformation. *AIAA Paper 2004-4630*, 2004.
- <sup>27</sup>John C. Vassberg, Mark A. DeHaan, S. Melissa Rivers, and Richard A. Wahls. Development of a common research model for applied cfd validation studies. *AIAA*, (2008-6919), 2008.
- <sup>28</sup>Zhoujie Lyu, Gaetan K. W. Kenway, and Joaquim R. R. A. Martins. Aerodynamic shape optimization investigations of the common research model wing benchmark. *AIAA Journal*, 2014. (In press).
- <sup>29</sup>S. Chen, Z. Lyu, G. K. Kenway, and J. Martins. Aerodynamic shape optimization of the common research model wing-body-tail configuration. *AIAA Paper 2015-1718*, 2015.
- <sup>30</sup>Sebastian A. Illi, Christian Fingskes, Thorsten Lutz, and Ewald Krämer. Transonic tail buffet simulation for the common research model. *AIAA Applied Aerodynamics Conference*, (2013-2510), June 2013.
- <sup>31</sup>Anthony J. Sclafani, Mark A. DeHaan, John C. Vassberg, Christopher L. Rumsey, and Thomas H. Pulliam. Drag prediction for the nasa crm wing-body-tail using cfl3d and overflow on an overset mesh. *AIAA Applied Aerodynamics Conference*, (2010-4219), 2010.
- <sup>32</sup>Melissa B. Rivers and Ashley Dittberner. Experimental investigations of the nasa common research model in the nasa langley national transonic facility and nasa ames 11-ft transonic wind tunnel (invited). *AIAA Aerospace Sciences Meeting*, (2011-1126), January 2011.